ELSEVIER

Journal of Fluids and Structures 22 (2006) 441–461

JOURNAL OF FLUIDS AND STRUCTURES

www.elsevier.com/locate/jfs

An unstructured-mesh-based finite element simulation of wave interactions with non-wall-sided bodies

C.Z. Wang, G.X. Wu*

Department of Mechanical Engineering, University College London, Torrington Place, London WC1E 7JE, UK

Received 13 May 2005; accepted 27 December 2005
Available online 9 March 2006

Abstract

An unstructured-mesh-based finite element method is employed to simulate two-dimensional nonlinear interactions between waves and non-wall-sided floating structures. The velocity potential theory is adopted and the potential is obtained at each time step through solving a matrix equation based on the Galerkin method. The boundary conditions on the free surface are satisfied in the Lagrangian form and the information is updated through the fourth-order Runge–Kutta method. Remeshing based on B-splines is applied regularly to avoid over-distorted elements, and smoothing based on a method using the energy of a curve defined through its nodes is applied to improve the stability of the results. Comparison is made with published results for transient wave motion in a tank to validate the present method. Extensive simulation is made for wedge-shaped bodies in vertical and horizontal motions, and comparison is made with the solution from second-order theory. Results are also provided for wedges in a tank, for wedges in large motion relative to water depth and for twin wedges.

Keywords: Unstructured mesh; Finite element method; Nonlinear water waves; Non-wall-sided bodies

1. Introduction

In the last decade, there have been extensive applications of the finite element method (FEM) to fully nonlinear wave–body interaction problems. Wu and Eatock Taylor (1994) used both the FEM and the mixed FEM to analyze the two-dimensional (2-D) nonlinear transient water wave problems. Wu and Eatock Taylor (1995) subsequently made detailed comparison between FEM and the boundary element method (BEM) for the nonlinear free surface flow problem and found that the former was more efficient in terms of both CPU and memory requirement. Later, Ma et al. (2001a, b) extended the technique to simulate interactions between waves and 3-D fixed structures in numerical tanks, and Hu et al. (2002) to the case of a vertical cylinder in forced motions. Robertson and Sherwin (1999) adopted an hp-element technique to simulate the 2-D free surface flow problem. Recently, the FEM was also used by Robertson et al. (2004) for 2-D free-surface flow problems with viscous effects. Other FEM-based simulations include those by Clauss and Steinhagen (1999), Westhuis (2001) and Wang and Khoo (2005).

The publications mentioned above have mainly used structured meshes. A structured mesh is easier to generate but may become ineffective if the fluid domain is complex due to the geometry of the body or large motion of the

*Corresponding author. Tel.: +44 20 7679 3870; fax: +44 20 7388 0180.
E-mail address: gx_wu@meng.ucl.ac.uk (G.X. Wu).

0889-9746/$ - see front matter © 2006 Elsevier Ltd. All rights reserved.
doi:10.1016/j.jfluidstructs.2005.12.005

boundaries. In this case, an unstructured mesh will be more suitable. Greaves et al. (1997) employed quad-tree-based unstructured meshes to model fully nonlinear waves. Zhu et al. (2001) used a similar meshing procedure to simulate interactions of submerged cylinders and viscous flow with a free surface. Turnbull et al. (2003) adopted a coupled structured and unstructured mesh technique to simulate 2-D wave–body interactions. In 3-D, Wu and Hu (2004) used an unstructured mesh in the horizontal plane and a structured mesh in the vertical direction.

All these applications are either for submerged bodies or for wall-sided floating bodies where the body surface at the moving waterline is always vertical to the still water level. In fact, the nonlinear effect will become more significant for a non-wall-sided body. From the computational point, the presence of the flare makes the mesh generation more complex, especially in the area near the intersection of the body surface and the free surface. The slope or the curvature of the body near the waterline also makes it more difficult to trace the movement of the waterline in the nonlinear simulation. In this paper, we use a mesh generator called BAMG (Hecht, 1998) to generate an unstructured mesh in the fluid domain. It is based on the Delaunay algorithm and needs information only on the boundary as the input. Simulations are first made for wave motions in a rectangular tank and for progressive waves in a numerical tank, and results are compared with published data for validation. The focus of this work is on a wedge either in forced large amplitude motion or in nonlinear waves in a numerical tank, and on twin wedges. The wedge has been widely investigated for the water entry problem and an extensive survey of the work in this area has been given in Wu et al. (2004). This is a good example of a non-walled body, and results for this case can provide valuable information on the nature of wave interactions with some complicated body shapes.

2. Mathematical formulation

The 2-D problem considered here is illustrated in Fig. 1 which shows a floating body oscillating with large amplitude in otherwise calm water. A Cartesian coordinate system is defined so that the x-axis coincides with the undisturbed free surface and the y-axis is positive upwards. The free surface and the body surface are denoted as S_f and S_b, respectively. The seabed is assumed horizontal along the plane $y = -h$. With the fluid assumed incompressible and inviscid, and the flow irrotational, the fluid motion can be described by a velocity potential ϕ, which satisfies the Laplace equation within the fluid domain Ω, or

$$\nabla^2\phi = 0 \qquad \text{in } \Omega. \tag{1}$$

The boundary conditions on the instantaneous free surface S_f or $y = \eta$ can be written as

$$\frac{\partial\phi}{\partial t} + g\eta + \frac{1}{2}|\nabla\phi|^2 = 0 \qquad \text{on } S_f, \tag{2}$$

$$\frac{\partial\phi}{\partial y} - \frac{\partial\eta}{\partial t} - \frac{\partial\phi}{\partial x}\frac{\partial\eta}{\partial x} = 0 \qquad \text{on } S_f, \tag{3}$$

where t and g denote time and acceleration due to gravity, respectively. These equations can also be written in the Lagrangian form

$$\frac{\mathrm{d}\phi}{\mathrm{d}t} = -g\eta + \frac{1}{2}\nabla\phi\nabla\phi, \tag{4}$$

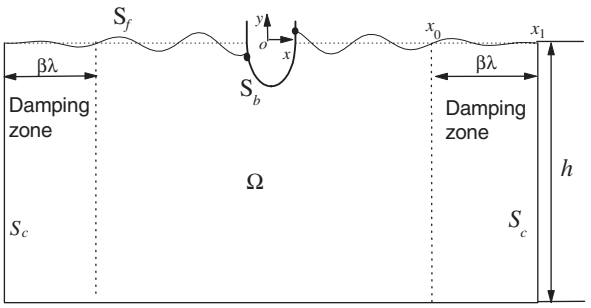

Fig. 1. Coordinate system.

$$\frac{dx}{dt}=\frac{\partial\phi}{\partial x},\quad \frac{dy}{dt}=\frac{\partial\phi}{\partial y}. \tag{5}$$

On the body surface, the boundary condition can be given as

$$\frac{\partial\phi}{\partial n}=V_n \qquad \text{on } S_b, \tag{6}$$

where V_n is the body surface velocity in its normal direction $\vec{n}=(n_x,n_y)$ which is positive away from the fluid domain. To satisfy the radiation condition, an artificial damping zone is employed to absorb the incoming wave and minimize the reflection. This is achieved through adding a damping term in Eqs. (4) and (5), or

$$\frac{d\phi}{dt}=-g\eta+\frac{1}{2}\nabla\phi\nabla\phi-\nu(x)\phi, \tag{7}$$

$$\frac{dx}{dt}=\frac{\partial\phi}{\partial x},\quad \frac{dy}{dt}=\frac{\partial\phi}{\partial y}-\nu(x)y, \tag{8}$$

where $\nu(x)$ is the damping coefficient

$$\nu(x)=\begin{cases}\alpha\omega\left(\dfrac{|x|-x_0}{\lambda}\right)^2 & \text{for } x_0\leqslant|x|\leqslant x_1=x_0+\beta\lambda,\\ 0 & \text{for } |x|<x_0;\end{cases}$$

ω and λ in the last equation are a wave frequency and linear wavelength, respectively, and α and β can be taken as 1 as suggested by Tanizawa and Swada (1996) based on their numerical experiment. When the damping zone is efficient over its length $\beta\lambda$, there should be no wave of significance remaining at the far end. Thus the boundary condition on S_c can be written as

$$\frac{\partial\phi}{\partial n}=0 \qquad \text{on } S_c. \tag{9}$$

To complete the boundary value problem, the initial condition is given as

$$\phi(x,y=\xi,t=0)=\phi_0(x),\quad \eta(x,t=0)=\xi(x), \tag{10}$$

in which ϕ_0 and ξ are known functions.

Once the potential is found, the pressure in the fluid may be obtained from the Bernoulli equation,

$$p=-\rho\left(\frac{\partial\phi}{\partial t}+\frac{1}{2}|\nabla\phi|^2+gy\right). \tag{11}$$

The hydrodynamic force acting on the body can be expressed as

$$\vec{F}=\int_{S_b}p\vec{n}\,ds. \tag{12}$$

In this equation, the derivative of velocity potential ϕ with respect to time t is not explicitly given, even when the potential itself has been found at each time step. It could be calculated by a backward finite difference method. This, however, is not always convenient when remeshing is applied and could cause instability for the motion of a free-floating body as it leads to many spikes in the force history. Here we use the method developed by Wu and Eatock Taylor (1996, 2003). They introduced some auxiliary functions to circumvent the need of calculating the derivative of the potential with respect to time so that the force can be found directly before the pressure itself is known.

3. Numerical procedures

An essential part of CFD simulations is the mesh generation. Here the 2-D unstructured mesh is generated using a 2-D generator called BAMG (Hecht, 1998). It is based on the Delaunay algorithm and is found to be suitable for handling complex geometry shapes. It needs element information on the boundary, which includes its number and the coordinates of two nodes at both ends. A typical unstructured triangular mesh for a floating wedge is shown in Fig. 2.

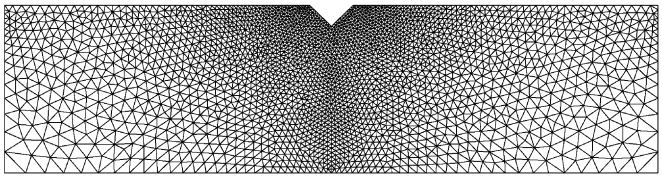

Fig. 2. An unstructured mesh for a floating wedge.

After the mesh is generated, the velocity potential ϕ can be expanded in terms of the shape function $N_J(x,y)$:

$$\phi = \sum_{J=1}^{n} \phi_J N_J(x,y), \tag{13}$$

where ϕ_J is the velocity potential at node J and n is the number of nodes. Based on the Galerkin method, we have

$$\int\int_{\Omega} \nabla^2 \phi N_I \, \mathrm{d}\Omega = 0.$$

From Green's identity and the boundary conditions, this equation becomes

$$\int\int_{\Omega} \nabla N_I \sum_{\substack{J=1 \\ (J \notin S_P)}}^{n} \phi_J \nabla N_J \, \mathrm{d}\Omega = \int_{S_n} N_I f_n \, \mathrm{d}S$$
$$- \int\int_{\Omega} \nabla N_I \sum_{\substack{J=1 \\ (J \in S_P)}}^{n} (f_P)_J \nabla N_J \mathrm{d}\Omega \quad (I \notin S_p), \tag{14}$$

where S_p represents the Dirichlet boundary on which the velocity potential, denoted by f_p, is known, and S_n represents the Neumann boundary on which the normal derivative of the velocity potential, denoted by f_n, is known. The equation can further be written in the matrix form:

$$[K]\{\phi\} = \{F\}, \tag{15}$$

where

$$\{\phi\} = [\phi_1, \phi_2, \ldots, \phi_I, \ldots, \phi_n]^{\mathrm{T}} \quad (I \notin S_p),$$

$$K_{IJ} = \int\int_{\Omega} \nabla N_I \nabla N_J \, \mathrm{d}\Omega \quad (I \notin S_p \ \& \ J \notin S_p),$$

$$F_I = \int_{S_n} N_I f_n \, \mathrm{d}S - \int\int_{\Omega} \nabla N_I \sum_{\substack{J=1 \\ (J \in S_p)}}^{n} (f_p)_J \nabla N_J \, \mathrm{d}\Omega \quad (I \notin S_p).$$

This linear matrix equation is then solved through the conjugate gradient (CG) method with a symmetric successive over-relaxation (SSOR) preconditioner.

The global matrix $[K]$ is generally sparse and symmetric. In order to take advantage of the fact that there is a large number of zero elements, we use the compressed sparse row (CSR) format to store $[K]$. A data structure called a linked list (Dale, 1998) is very convenient and efficient for storing the nonzero elements in $[K]$. Each node in the list contains the column number and value of the nonzero element. The index system can be easily obtained from the list using assignment and addition operations.

After the potential is obtained by solving Eq. (15), the velocity can be obtained by using the procedure developed by Wu and Eatock Taylor (1994). We first expand the velocity in a manner similar to that in Eq. (13). The Galerkin method is then applied to $\vec{u} = \nabla\phi$, which means

$$\int\int_{\Omega} (\vec{u} - \nabla\phi) N_I \mathrm{d}\Omega = 0. \tag{16}$$

This gives

$$\int\int_{\Omega} \vec{u} N_I \, d\Omega = \int\int_{\Omega} \nabla\phi N_I \, d\Omega, \tag{17}$$

which in matrix form becomes

$$[A]\{\vec{u}\} = [\vec{B}]\{\phi\}, \tag{18}$$

where

$$A_{IJ} = \int\int_{\Omega} N_I N_J \, d\Omega, \quad \vec{B}_{IJ} = \int\int_{\Omega} N_I \nabla N_J \, d\Omega.$$

Eq. (18) can be solved through a procedure similar to that used for Eq. (15).

The fourth-order Runge–Kutta method is adopted for the integration with respect to time to up-date the wave elevation and the potential on the free surface. This method is particularly advantageous when remeshing is used regularly. For other methods of similar order of accuracy, information at the last few time steps is required, which can be problematic if they all correspond to different meshes. The Runge–Kutta method uses mini steps within each time step and all the information required for integration over the time step corresponds to the same mesh.

Let P denote one of these three variables (x,y,ϕ). If P^n is the value at time step $n\Delta t$, the new value at $t = (n+1)\Delta t$ can be obtained through the following equation (Engeln-Müllges and Uhlig, 1996):

$$P^{n+1} = P^n + \frac{\Delta t}{8}(k_1 + 3k_2 + 3k_3 + k_4), \tag{19}$$

where

$$k_i = \frac{d}{dt}\left[P\left(n\Delta t + \frac{i-1}{3}\Delta t, Q^{n+(i-1)/3}\right)\right] \quad (i = 1,2,3,4)$$

and

$$Q^n = P^n, \;\; Q^{n+1/3} = P^n + \frac{\Delta t}{3}k_1,$$

$$Q^{n+2/3} = P^n + \Delta t\left(-\frac{1}{3}k_1 + k_2\right), \;\; Q^{n+1} = P^n + \Delta t(k_1 - k_2 + k_3).$$

When the simulation is over a substantial period of time, the nodes on the free surface may cluster or stretch. In order to avoid over-distortion of elements, nodes on the free surface should be rearranged every several time steps. We adopt the following procedure, results from which are shown in Fig. 3 by way of example. Suppose there are $n+1$ nodes $\mathbf{P}_i$ (x_i,y_i) $(i = 0,1,\ldots,n)$ on a curve. We may interpolate any point on the curve between nodes $\mathbf{P}_i$ and $\mathbf{P}_{i+1}$ using B-splines. We use the uniform cubic B-spline to express the point as

$$\mathbf{P}(u) = \sum_{j=0}^{3} B_{j,3}(u)\mathbf{V}_{i+j} \quad (i = 0,1,\ldots,n), \tag{20}$$

where u varies from 0 at i to 1 at $i+1$; $B_{j,3}(u)$ are cubic B-spline functions and may be expressed as

$$B_{0,3}(u) = \frac{1}{6}(1-u)^3, \;\; B_{1,3}(u) = \frac{1}{6}(3u^3 - 6u^2 + 4),$$
$$B_{2,3}(u) = \frac{1}{6}(-3u^3 + 3u^2 + 3u + 1), \;\; B_{3,3}(u) = \frac{1}{6}u^3, \tag{21}$$

and $\mathbf{V}_{i+j}$ are control points. The whole curve is then forced to pass through all the points $\mathbf{P}_i$, which means

$$\mathbf{P}_i(0) = \frac{1}{6}(\mathbf{V}_i + 4\mathbf{V}_{i+1} + \mathbf{V}_{i+2}) \quad (i = 0,1,\ldots,n). \tag{22}$$

In matrix from, this becomes

$$[A][\mathbf{V}] = [\mathbf{P}], \tag{23}$$

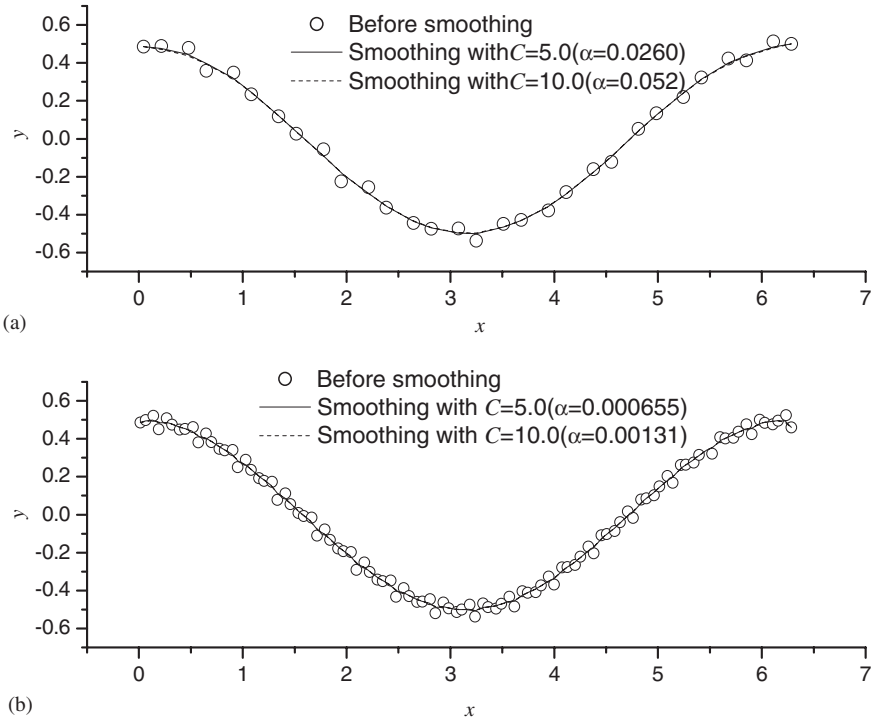

Fig. 3. Curve smoothing: (a) 30 nodes and $l_{\min} = 0.173$; (b) 100 nodes and $l_{\min} = 0.051$.

where $[A]$ is a tridiagonal matrix, $[\mathbf{V}]$ and $[\mathbf{P}]$ are vectors consisting of the control points $\mathbf{V}_i$ and nodes $\mathbf{P}_i$, respectively,

$$[A] = \begin{bmatrix} 6 & 0 & & & & \\ 1 & 4 & 1 & & & \\ & 1 & \ddots & \ddots & & \\ & & \ddots & \ddots & 1 & \\ & & & \ddots & 4 & 1 \\ & & & & 0 & 6 \end{bmatrix}, \quad [\mathbf{V}] = \begin{bmatrix} \mathbf{V}_0 \\ \mathbf{V}_1 \\ \vdots \\ \mathbf{V}_{n+2} \end{bmatrix}, \quad [\mathbf{P}] = 6 \begin{bmatrix} \mathbf{P}_{-1} \\ \mathbf{P}_0 \\ \vdots \\ \mathbf{P}_{n+1} \end{bmatrix}.$$

The boundary points $\mathbf{V}_0$ and $\mathbf{V}_{n+2}$ are set to be $\mathbf{P}_{-1}$ and $\mathbf{P}_{n+1}$, respectively, and $\mathbf{P}_{-1}$ and $\mathbf{P}_{n+1}$ may be obtained from

$$\mathbf{P}_{-1} = 2\mathbf{P}_0 - \mathbf{P}_1, \quad \mathbf{P}_{n+1} = 2\mathbf{P}_n - \mathbf{P}_{n-1}.$$

The arc length from node $\mathbf{P}_i$ to $\mathbf{P}_0$ may be calculated by the following equation:

$$S_i = \sum_{k=0}^{i} \int_0^1 \left(\frac{\mathrm{d}s}{\mathrm{d}u}\right)_k \mathrm{d}u \quad (i = 0, 1, \ldots, n), \tag{24}$$

where

$$\left(\frac{\mathrm{d}s}{\mathrm{d}u}\right)_i = \sqrt{\left(\frac{\mathrm{d}x}{\mathrm{d}u}\right)^2 + \left(\frac{\mathrm{d}y}{\mathrm{d}u}\right)^2} \text{ and } \left(\frac{\mathrm{d}x}{\mathrm{d}u}, \frac{\mathrm{d}y}{\mathrm{d}u}\right) = \frac{\mathrm{d}\mathbf{P}(u)}{\mathrm{d}u} = \sum_{j=0}^{3} \frac{\mathrm{d}B_{j,3}}{\mathrm{d}u} \mathbf{V}_{i+j}.$$

We then divide the curve into m segments. The size of each segment can be chosen based on the local flow character. If we wish to have smaller elements near $\mathbf{P}_0$ and larger elements near $\mathbf{P}_n$ for example, we can adopt the following procedure (Chung, 2002). Suppose that the new nodes are $\mathbf{P}_{i,r} (i = 0, 1, \ldots, m)$. The arc length $S_{i,r}$ from node $\mathbf{P}_{0,r}$ to $\mathbf{P}_{i,r}$

can be obtained from

$$S_{i,r} = S_n \frac{(\beta+1)-(\beta-1)\left[(\beta+1/\beta-1)\right]^{1-i/m}}{\left[(\beta+1/\beta-1)\right]^{1-i/m}+1} \quad (i=0,1,\ldots,m), \tag{25}$$

where $\beta>1$ is a constant and it controls distribution of the nodes. A larger value of β will give a more uniform distribution.

In addition to node clustering and stretching, it is not unusual to see saw-tooth behaviour in the time domain simulations of water waves. Longuet-Higgins and Cokelet (1976) used the following smoothing scheme:

$$\bar{f}_i = \frac{1}{16}(-f_{i-2}+4f_{i-1}+10f_i+4f_{i+1}-f_{i+2}) \tag{26}$$

to eliminate such behaviour. But this is applicable only to nodes with equal spacing in the x direction. Here the distribution of nodes is irregular, and we shall use the following energy method for smoothing (Zhu, 2000). Suppose there is a discrete set of nodes defined through position vectors $\mathbf{Q}_i$ ($i=0,1,\ldots,n$), and nodes $\mathbf{Q}_i$ become $\mathbf{P}_i$ after smoothing. We define the energy of a curve with nodes $\mathbf{P}_i$ (i = 0,1,…,n) as

$$E_c = \sum_{j=1}^{n-1} \frac{1}{l_i+l_{i+1}}(e_{i+1}-e_i)^2, \tag{27}$$

where $l_i = \left\|\mathbf{Q}_i - \mathbf{Q}_{i-1}\right\|$ is the distance between $\mathbf{Q}_i$ and $\mathbf{Q}_{i-1}$; e_i in Eq. (27) is defined as $e_i = (p_i - p_{i-1})/l_i$, where $p_i(i=0,1,\ldots,n)$ is either the x or y coordinate of node $\mathbf{P}_i$. The smoothing process should ensure that the difference between $\mathbf{P}_i$ and $\mathbf{Q}_i(i=0,1,\ldots,n)$ is as little as possible. In order to achieve this, we define an objective function as

$$F_c = \alpha E_c + \sum_{j=0}^{n} \beta_j (p_j - q_j)^2, \tag{28}$$

where α and β_j are constants, $q_i(i=0,1,\ldots,n)$ is either the x or y coordinate of node $\mathbf{Q}_i$. Substituting Eq. (27) into Eq. (28), we obtain

$$F_c = \alpha \sum_{j=1}^{n-1} \frac{1}{l_{j+1}+l_j}\left(\frac{p_{j+1}-p_j}{l_{j+1}} - \frac{p_j - p_{j-1}}{l_j}\right)^2 + \sum_{j=0}^{n} \beta_j (p_j - q_j)^2. \tag{29}$$

The first summation of this equation reflects the smoothness, while the second summation reflects the difference between the curves before smoothing and after smoothing. Both of them should be minimal, which is achieved through setting the derivatives of F_c with respect to $p_i(i=0,1,\ldots,n)$ equal to zero. This gives

$$[A][\mathbf{P}] = [\mathbf{Q}], \tag{30}$$

where A is a matrix with a bandwidth of five,

$$A = \begin{bmatrix} c_0 & d_0 & e_0 & & & & \\ b_1 & c_1 & \ddots & \ddots & & & \\ a_2 & \ddots & \ddots & \ddots & \ddots & & \\ & \ddots & \ddots & \ddots & \ddots & e_{n-2} & \\ & & \ddots & \ddots & \ddots & d_{n-1} & \\ & & & a_n & b_n & c_n & \end{bmatrix}.$$

In our simulations, the constants β_j are set to be a unit value. The smoothing factor α is related to l_i ($i=1,\ldots,n$) and may be obtained by numerical tests. We adopt the following procedure. Suppose the minimum value of l_i ($i=1,\ldots,n$) is $l_{\min}$, we write $\alpha = C l_{\min}^3$ where C is a coefficient. Numerical tests in Fig. 3 show that a number between 5 and 10 is a good choice for C. It should also be mentioned that the boundary nodes $\mathbf{Q}_0$ and $\mathbf{Q}_n$ are constrained and they are equal to $\mathbf{P}_0$ and $\mathbf{P}_n$, respectively, which may be achieved simply by taking $d_0 = e_0 = a_n = b_n = 0$.

4. Numerical results

Simulations based on the above procedure are first made for wave motions in a rectangular tank and for progressive waves in a numerical tank. The results obtained are compared with published data for validation. Extensive simulations are then made for a wedge in a tank, and for single and twin wedges in forced motions. The second-order theory is also used in several cases for comparison.

4.1. Free oscillation problems

The first validation case concerns a free oscillation problem in a rectangular container with length L and depth $h = L/2$, as shown in Fig. 4. The initial wave elevation and the velocity potential on the free surface are given as

$$\eta(x, t = 0) = A\cos(2\pi x/L),$$

$$\phi(x, \eta(x, 0), t = 0) = 0,$$

respectively, where A is the wave amplitude. The analytical solutions of first- and second-order wave elevation at $x = L/2$ for this case have been given by Wu and Eatock Taylor (1994)

$$\eta^{(1)}(x, t) = a\cos(\omega_2 t)\cos(k_2 x), \tag{31}$$

$$\eta^{(2)}(x = L/2, t) = \frac{1}{8g}\left[2(\omega_2 A)^2\cos 2\omega_2 t) + \frac{A^2}{\omega_2^2}(k_2^2 g^2 + \omega_2^4) - \frac{A^2}{\omega_2^2}(k_2^2 g^2 + 3\omega_2^4)\cos \omega_4 t)\right], \tag{32}$$

where

$$k_i = i\pi/L \quad (i = 1, 2, 3, \ldots),\ \omega_i = [k_i g\tanh(k_i h)]^{1/2} \quad (i = 1, 2, 3, \ldots).$$

This result will be used for validation below.

In the simulation, the finite element nodes are uniformly distributed along the free surface and the bottom of the container. A procedure similar to Eq. (25) is used along the depth to have smaller elements near the free surface. An initial mesh is shown in Fig. 5 with $NF = 120$ uniform segments on the free surface, $NB = NF/2$ uniform segments on the bottom and $NH = 40$ nonuniform segments on the side walls. Two cases at $A/h = 0.05$ and 0.1 are considered. The step of nondimensional time $\tau = t/\sqrt{h/g}$ is set to be 0.05 for the former and 0.025 for the latter. It is found that smoothing needs to be applied regularly. The mesh at $\tau = 4.9$ without smoothing is shown in Fig. 6, and the simulation crashes subsequently. When smoothing is applied every 20 time steps, the result becomes stable and the mesh at $\tau = 12$ is shown in Fig. 7. The numerical results with two different meshes are shown in Fig. 8, together with the linear solution plus the second-order solution obtained from Eqs. (31) and (32). The figure suggests that the numerical simulation is convergent and provides good accuracy.

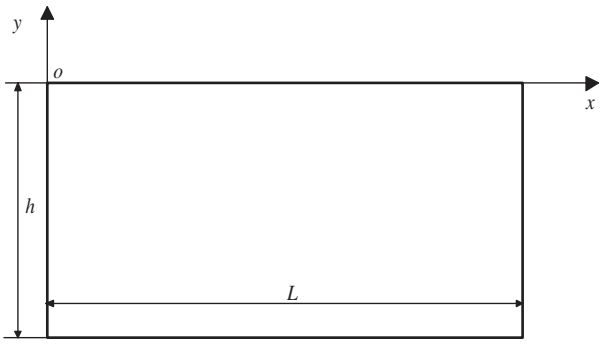

Fig. 4. Sketch of a container.

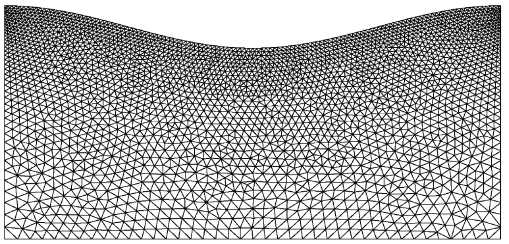

Fig. 5. An initial mesh for a container with 2807 nodes and 5372 elements.

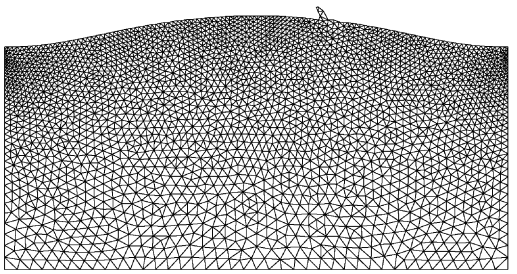

Fig. 6. Mesh at $\tau = 4.9$ without smoothing.

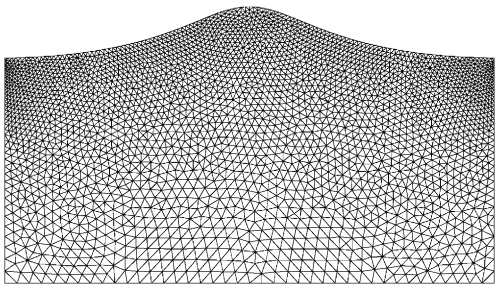

Fig. 7. Mesh at $\tau = 12$ with smoothing.

4.2. Wave tank problems

We next consider wave propagation generated by a piston-type wave maker installed at the left-hand side of a numerical tank. The wave-maker undergoes motion with the following horizontal velocity:

$$U(t) = \omega A \cos \omega t, \tag{33}$$

where ω and A are the motion frequency and amplitude of the wave-maker, respectively. The case chosen is that studied by Lin et al. (1984) with $h = 0.6\,\mathrm{m}$, $L = 9\,\mathrm{m}$, $A = 0.05h$ and $\omega = 1.5539\sqrt{g/h}$. An initial mesh with $NF = 200$, $NB = 150$, $NH = 20$ on the left-hand side of the tank and 16 on the right is shown in Fig. 9. This corresponds to 2423 nodes and 4458 elements. The damping zone is applied at the far end over one wave length. Fig. 10 gives the wave histories at $x = 1.167\ h = 0.078L$, where again x is measured from the left-hand end of the tank, with two different time steps, where $T = 2\pi/\omega$. It clearly shows that convergence in the time discretization has been achieved. The results have been compared visually with those by Lin et al. (1984) and no visible difference is found.

Further validation is made by making comparison between the present fully nonlinear result and the solutions obtained from the perturbation method. In this method the first- and second-order velocity potentials satisfy the Laplace equation in the fluid domain,

$$\nabla^2 \phi^{(k)} = 0 \ \ (k = 1, 2) \quad \text{in } \Omega^{(0)}, \tag{34}$$

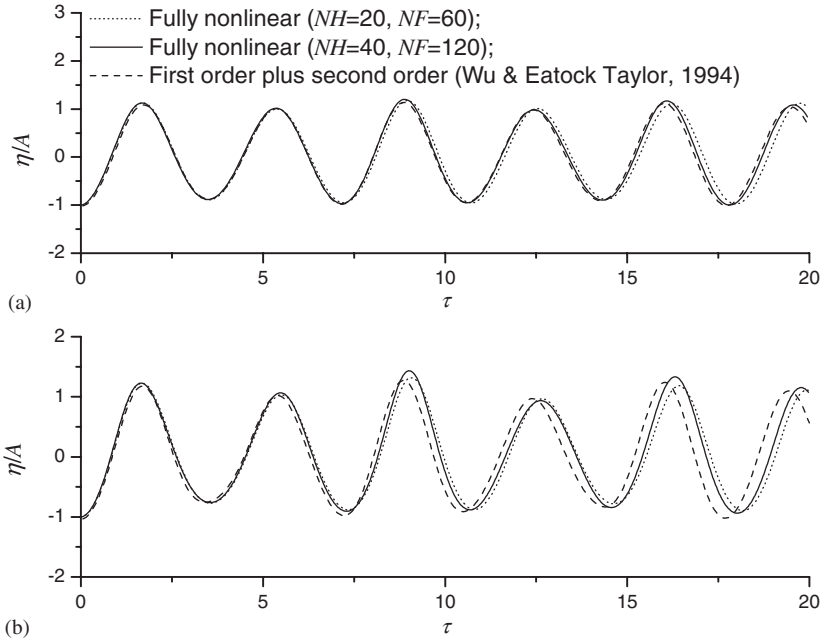

Fig. 8. Wave histories at $x/L = 0.5$: (a) $A/h = 0.05$; (b) $A/h = 0.1$.

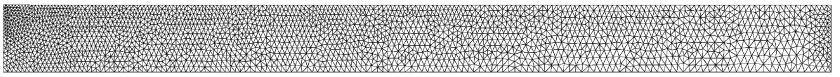

Fig. 9. An initial mesh with 2423 nodes and 4458 elements.

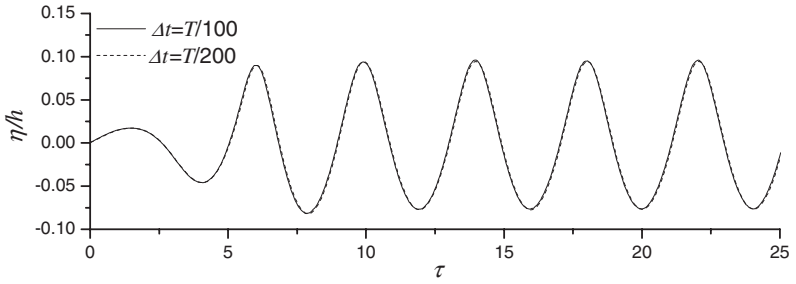

Fig. 10. Wave histories in the tank at $x = 1.167h$.

and they are subject to the conditions on the mean positions of the boundaries. They can be, given as

$$\frac{\partial \phi^{(k)}}{\partial y} - \frac{\partial \eta^{(k)}}{\partial t} = f'_k \quad \text{on } S_f^{(0)}, \tag{35}$$

$$\frac{\partial \phi^{(k)}}{\partial t} + g\eta^{(k)} = f''_k \quad \text{on } S_f^{(0)}, \tag{36}$$

$$\frac{\partial \phi^{(k)}}{\partial n} = f_k \quad \text{on } S_w^{(0)}, \tag{37}$$

$$\frac{\partial \phi^{(k)}}{\partial y} = 0 \quad \text{on } y = -h, \tag{38}$$

where $\Omega^{(0)}$ is a time-independent fluid domain bounded by the tank bottom, the mean surface of the wave-maker $S_w^{(0)}$, the still water surface $S_f^{(0)}$ and the far end of the tank. The terms f'_k, f''_k and f_k are given, respectively, as

$$f'_k = \begin{cases} 0 & (k=1), \\ \dfrac{\partial \phi^{(1)}}{\partial x}\dfrac{\partial \eta^{(1)}}{\partial x} - \eta^{(1)}\dfrac{\partial^2 \phi^{(1)}}{\partial y^2} & (k=2), \end{cases}$$

$$f''_k = \begin{cases} 0 & (k=1), \\ -\dfrac{1}{2}\left|\nabla \phi^{(1)}\right|^2 - \eta^{(1)}\dfrac{\partial^2 \phi^{(1)}}{\partial y\,\partial t} & (k=2), \end{cases}$$

$$f_k = \begin{cases} -U & (k=1), \\ X\dfrac{\partial^2 \phi^{(1)}}{\partial x^2} & (k=2), \end{cases}$$

where $X = A\sin \omega t$ is due to the motion of the wave-maker. The closure of this problem can be achieved by including the initial and the radiation conditions. It is then solved through the quadrilateral-based FEM with quadratic shape functions. For the wave tank problem, 80 segments in the horizontal direction and 7 in the vertical direction are used, which corresponds to 1855 nodes and 560 elements. The results are shown in Fig. 11 together with the fully nonlinear solution. It can be seen that the linear plus second-order solution is in very good agreement with the fully nonlinear result for this case.

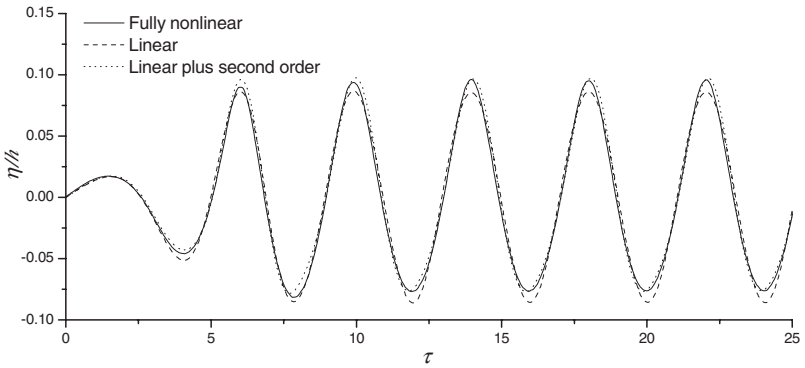

Fig. 11. Comparison of wave histories at $x = 1.167h$.

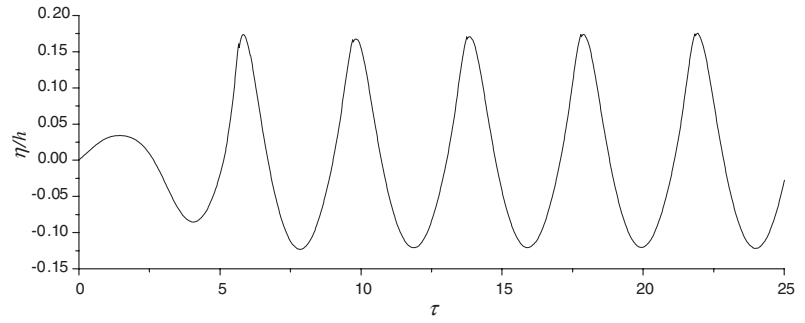

Fig. 12. Wave history in the tank at $A/h = 0.1$.

After these comparisons, a fully nonlinear simulation is made for the wave-maker at larger amplitude. A case at $A/h = 0.1$ is considered. The wave history at the same location as above is shown in Fig. 12 and the wave profile at $\tau = 24.26$ is shown in Fig. 13. As expected, the nonlinear features in these figures become more evident.

We now put a wedge in the tank at $x = 10h$. The body is symmetric about a vertical line and Fig. 14 shows half of the wedge. The case considered corresponds to $d = 0.4h$ and $\beta = 75^\circ$. The motion of the wave-maker still follows that defined in Eq. (33). The motion amplitude is taken as $A = 0.05h$ and the frequency remains the same. The wave profile at $\tau = 58.63$ is shown in Fig. 15. In the simulation, the wetted surface of the body may vary significantly with time, and the number of nodes on the surface will follow this change to ensure the sizes of the elements attached to the body will remain more or less the same.

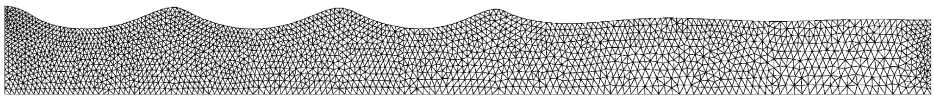

Fig. 13. Wave profile in the tank at $\tau = 24.26$ ($A/h = 0.1$).

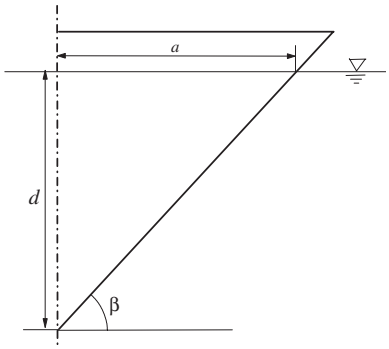

Fig. 14. Sketch of a floating wedge.

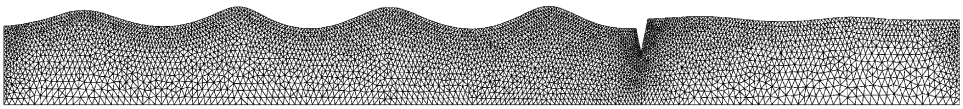

Fig. 15. Wave profile at $\tau = 58.63$.

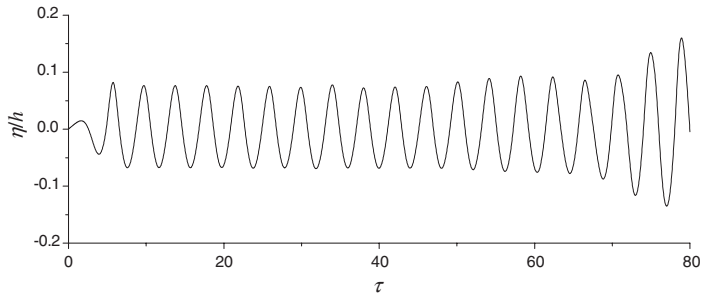

Fig. 16. Wave history at $x = 1.167h$.

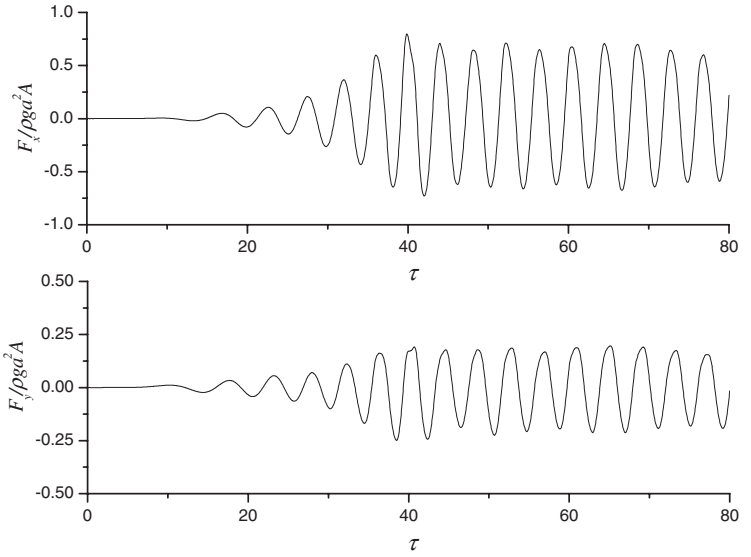

Fig. 17. History of force on a wedge in the tank.

The wave history at $x = 1.167h$ is shown in Fig. 16. The difference between this case and that in Fig. 10 is that waves will be reflected from the body after several periods. The corresponding hydrodynamic forces without the contribution of initial buoyancy are shown in Fig. 17, and they are obtained through the method in Wu and Eatock Taylor (1996, 2003).

4.3. Floating wedges in forced oscillation

The next case considered is a wedge undergoing motion with the following vertical or horizontal displacement

$$X = A \sin \omega t. \tag{39}$$

The centre-line of the wedge is taken as the y-axis. In order to avoid an abrupt start and allow a gradual development of the radiated potential, the body surface boundary condition is multiplied by the following modulation function, as used by Isaacson and Ng (1993)

$$M(t) = \begin{cases} \frac{1}{2}[1 - \cos(\pi t/2T)], & t < 2T, \\ 1, & t \geqslant 2T \quad \left(T = \frac{2\pi}{\omega}\right). \end{cases} \tag{40}$$

We take $d = h/8$, $\beta = 60^\circ$ and $A/d = 0.5$, which is relatively large motion. Two cases of vertical motion at $\omega = 2\sqrt{g/h}$ and $\omega = 3\sqrt{g/h}$ are calculated and the wave elevation at $x = -2d$ is shown in Fig. 18, where $\bar{\omega} = \omega/\sqrt{g/h}$. The length of the computational domain on each side of the body is 3λ (λ is the wavelength) and is divided into 100 intervals at the initial time step; 20 intervals are used on the initial body surface and 20 intervals are used along the depth. On the seabed, the number of intervals is two-fifths of that on the free surface. It should be noticed that the number of elements on the free surface and the body surface varies with time. The time step is taken as $T/100$. Smoothing and remeshing are applied every 20 steps. The nonlinearity at $\omega = 3\sqrt{g/h}$ is stronger, because this corresponds to a shorter wave.

Another simulated case corresponds to a wedge of $\beta = 45^\circ$ in vertical motion at $A/d = 0.5$ and $\omega = 2\sqrt{g/h}$. The wave histories are shown in Fig. 19. For the heave motion, the flow should be symmetric about the centre-line of the wedge. However, due to the asymmetric nature of the unstructured mesh, symmetry in results may not be achieved because of insufficient accuracy. We plotted the results at $x = \pm 2d$ in Fig. 19(a) and $x = \pm 3d$ in Fig. 19(b). The figures clearly show that the symmetry is accurately maintained. For the linear problem, the wave histories near and away from the body should all be sinusoidal when the motion has become fully periodic, even though their amplitudes may be different. When nonlinear effects are strong, the higher-order components become significant. The wave histories at different locations will have not only different amplitudes but also different shapes, as shown in Fig. 19.

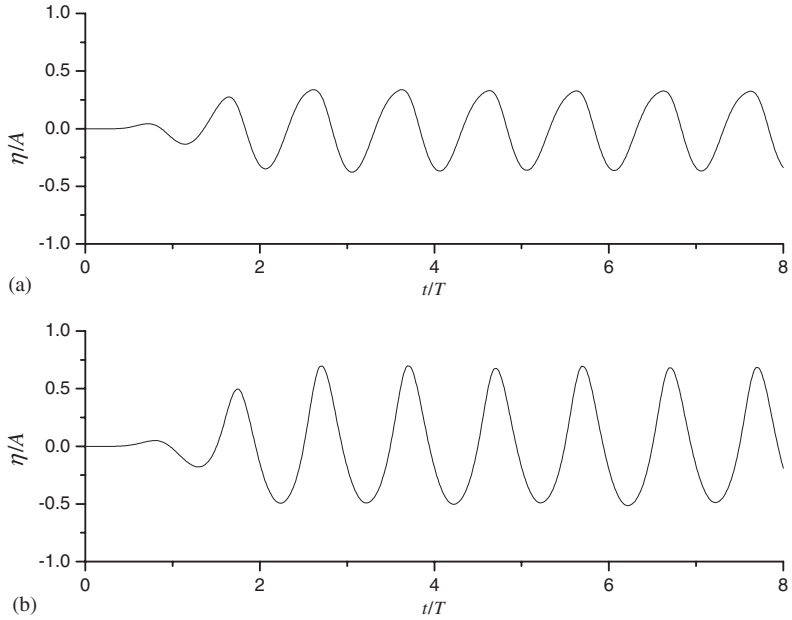

Fig. 18. Wave histories near the wedge with $\beta = 60^\circ$ in vertical motion ($x = -2d$ and $A/d = 0.5$): (a) $\bar{\omega} = 2.0$; (b) $\bar{\omega} = 3.0$.

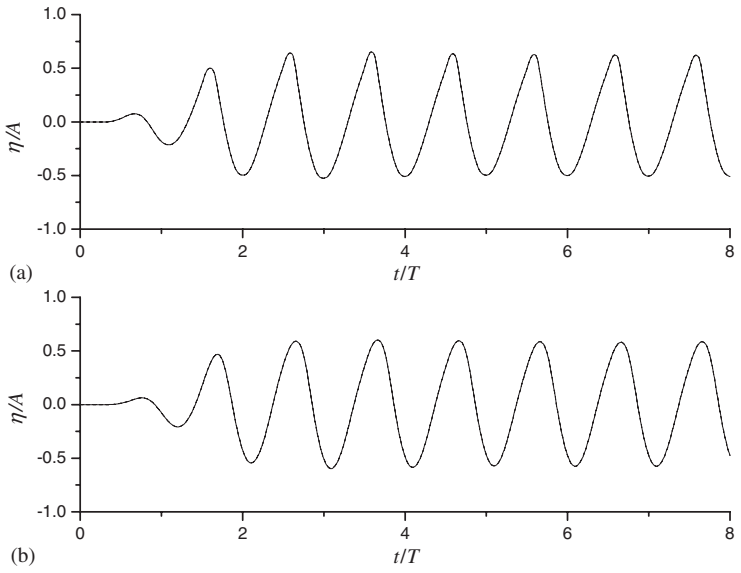

Fig. 19. Wave histories near the wedge with $\beta = 45^\circ$ in vertical motion ($\bar{\omega} = 2.0$ and $A/d = 0.5$): (a) $x = \pm 2d$; (b) $x = \pm 3d$.

To compare the present simulation with the result from the corresponding perturbation solution, the wedge with $\beta = 45^\circ$ in vertical motion is calculated here for several amplitudes. In this case, the second-order body surface boundary condition may be expressed as

$$\frac{\partial \phi^{(k)}}{\partial n} = f_k \quad \text{on } S_b^{(0)}, \tag{41}$$

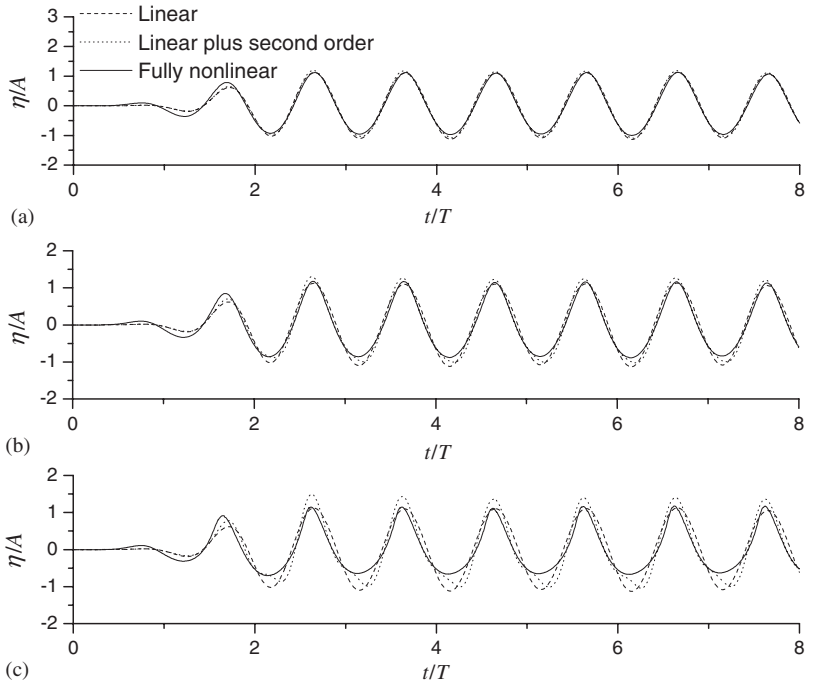

Fig. 20. Comparison of wave histories near the wedge with $\beta = 45^\circ$ in vertical motion ($x = -2d$ and $\bar{\omega} = 3.0$): (a) $A/d = 0.1$; (b) $A/d = 0.2$; (c) $A/d = 0.4$.

where $S_b^{(0)}$ is the mean body surface and f_k ($k = 1,2$) are given as

$$f_k = \begin{cases} \dfrac{\mathrm{d}X}{\mathrm{d}t} n_y & (k = 1), \\ -X\left(n_y \dfrac{\partial^2 \phi^{(1)}}{\partial y^2} + n_x \dfrac{\partial^2 \phi^{(1)}}{\partial x \partial y} \right) & (k = 2). \end{cases}$$

We consider a case with $\omega = 3\sqrt{g/h}$ at $A/d = 0.1,\ 0.2$ and 0.4. The waves at $x = -2d$ are given in Fig. 20. The figure shows that the results from the fully nonlinear solution and the perturbation theory are in good agreement at $A/d = 0.1$. Noticeable differences appear at $A/d = 0.2$ and become significant at $A/d = 0.4$. Further results from the nonlinear simulation for wave elevation at $x = -3d$ and for force are given in Fig. 21. The nonlinear features become very strong when the amplitude increases. Further simulation is made for a wedge of $\beta = 60^\circ$ in the identical condition. The results are shown in Fig. 22. The nonlinear features are still quite visible but weaker than those corresponding to $\beta = 45^\circ$, as the waterline is more 'wall-sided' in this case.

The case of a wedge of $\beta = 45^\circ$ in sway motion at $A/d = 0.5$ and $\omega = 2\sqrt{g/h}$ is also considered. The wave elevation and forces are shown in Figs. 23 and 24. It can be seen from Fig. 23 that the difference between phases of the wave histories at $x = -2d$ and $2d$ is about half a period. In fact, strictly speaking, after a sufficiently long period of time, these two curves should become identical if one of them is moved along the horizontal direction. This can be explained using the argument in Wu (1993, 2000). We can define z pointing out of the paper. One can view the same problem either along or against the z direction. The difference between these two cases is that there will be a phase difference of half a period when the problem becomes periodic. As a result, the horizontal force will have components at $(2n + 1)\omega$, while the vertical force components will be at $2n\omega$, ($n = 0,1,2\ldots$) This can be seen in Fig. 25. In fact, we may write

$$\frac{F}{\rho g d A} = \frac{a_0}{2} + \sum_{i=1}^{\infty} [A_i \cos(i\omega t) + B_i \sin(i\omega t)]. \tag{42}$$

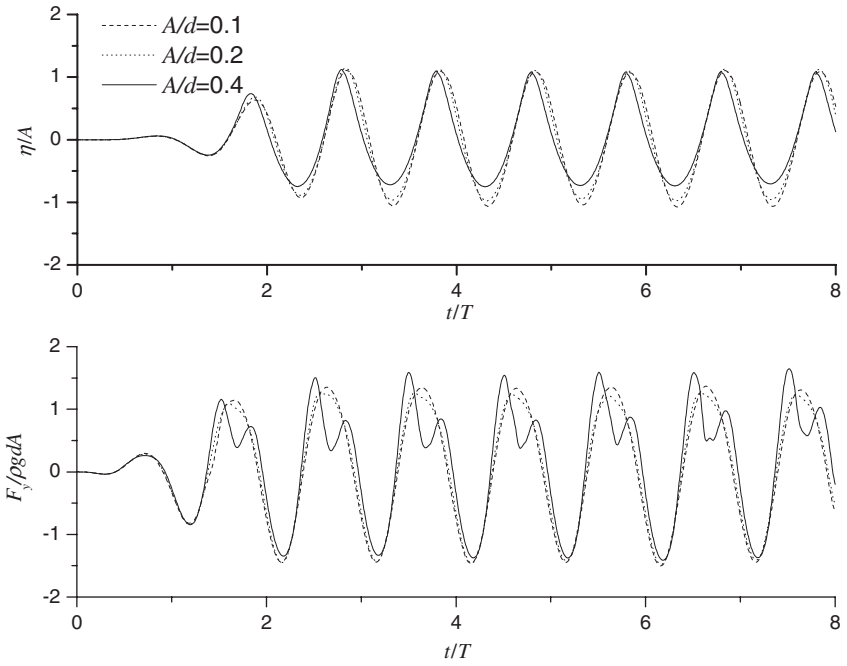

Fig. 21. Wave histories at $x = -3d$ and force histories for a wedge with $\beta = 45^\circ$ and $\bar{\omega} = 3.0$ in vertical motion.

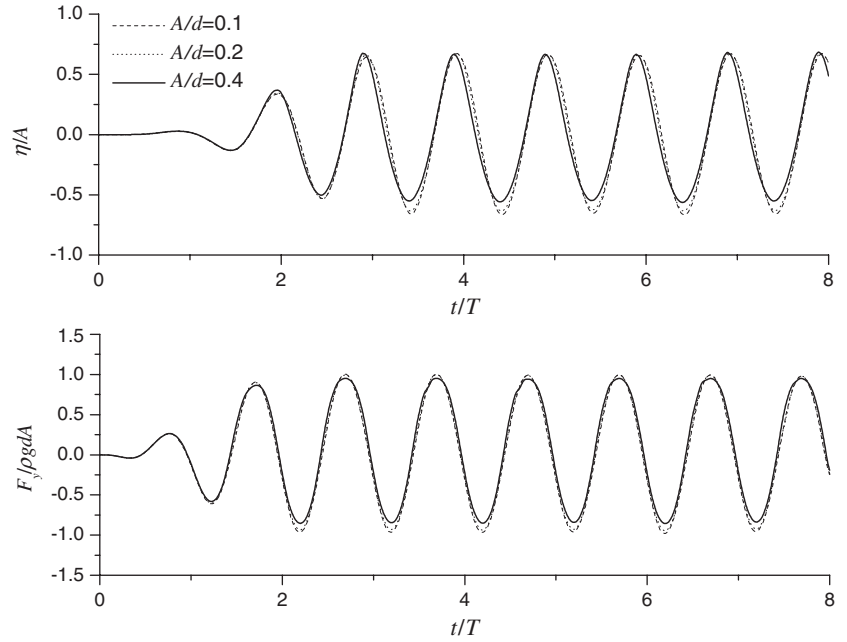

Fig. 22. Wave histories at $x = -3d$ and force histories for a wedge with $\beta = 60^\circ$ and $\bar{\omega} = 3.0$ in vertical motion.

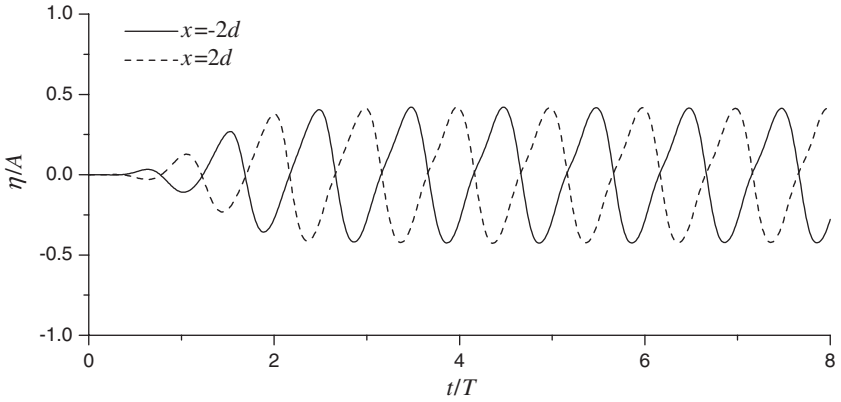

Fig. 23. Wave histories near the wedge in sway motion ($\bar{\omega} = 2.0$ and $A/d = 0.5$).

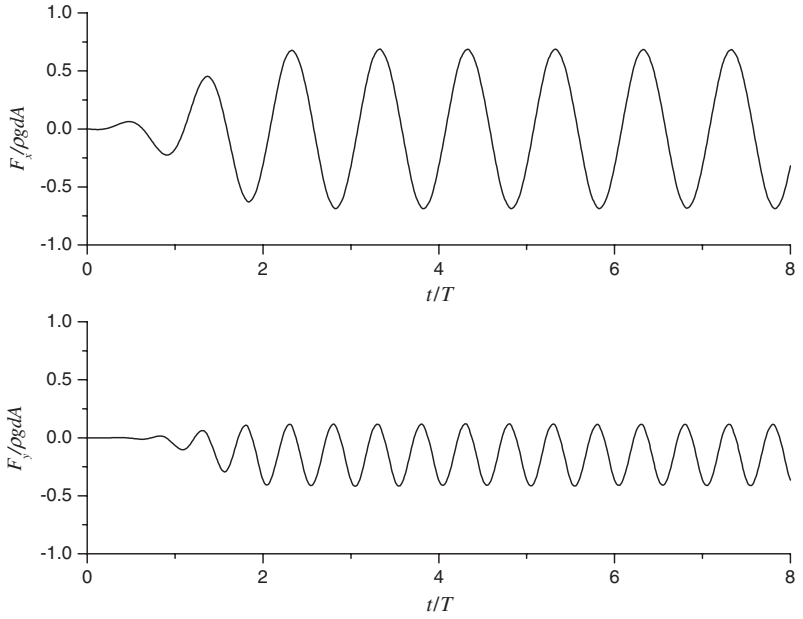

Fig. 24. Hydrodynamic forces on the wedge in sway motion ($\bar{\omega} = 2.0$ and $A/d = 0.5$).

The results using the Fourier analysis are shown in Fig. 25. It can be seen that the horizontal force is dominated by the component corresponding to $i = 1$, while the vertical force by $i = 0$ and 2.

A wedge in large heave motion relative to the water depth is also considered. In this case, the elements below the body can be squeezed or stretched, similar to the 3-D case considered by Wu and Hu (2004). It is vital that remeshing is applied regularly to avoid any over-distorted elements. We consider the case with $A/d = 0.4$, $\omega = 2\sqrt{g/h}$, $h = 2d$ and $\beta = 75^\circ$. This means that the distance from the tip of the wedge to the bottom of the fluid changes from $0.6d$ to $1.4d$. The wave history at $x = 2d$ is shown in Fig. 26 and the corresponding hydrodynamic force is given in Fig. 27. The wave is highly nonlinear. Some snapshots of the mesh at different time steps are shown in Fig. 28 and the result of remeshing is evident.

Twin-wedges are also considered here. Recently Wu (2006) solved the water entry problem for this case through a three-stage approach. He found that the pressure between the wedges can increase significantly as the wedges move into

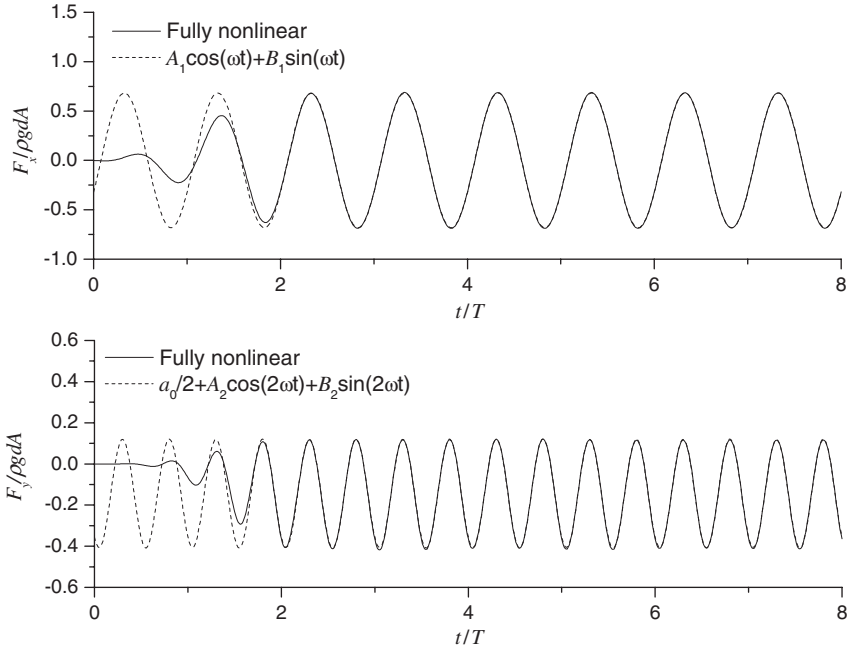

Fig. 25. Fully nonlinear results and Fourier components of the force.

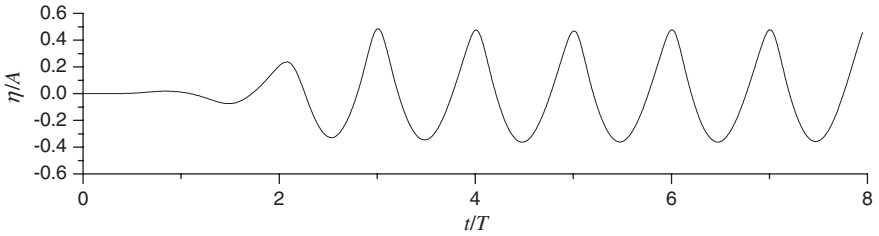

Fig. 26. Wave history at $x = 2d$.

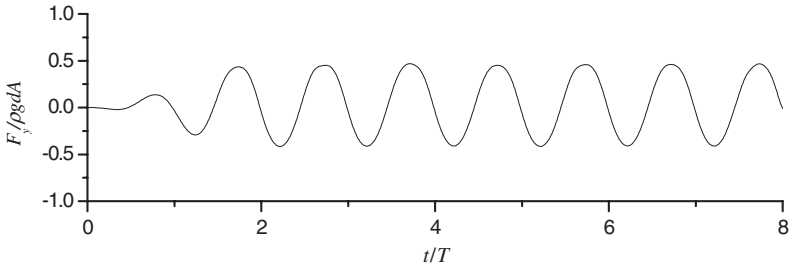

Fig. 27. Force history.

the water. Here both wedges have $\beta = 75^\circ$. The symmetry line of the two wedges is taken as the y-axis and the centrelines of the two bodies are located at $x = -1.5d$ and $1.5d$. The results for heave motion at$\omega = 2\sqrt{g/h}$, $A/d = 0.1$ and $h = 2d$ are shown in Figs. 29–31. The wave at $x = 0$ is much larger than those at $x = \pm 2d$, $\pm 3d$. The envelope of its amplitude is also very different. In fact it resembles to some extent the motion of sloshing waves in a tank, which is

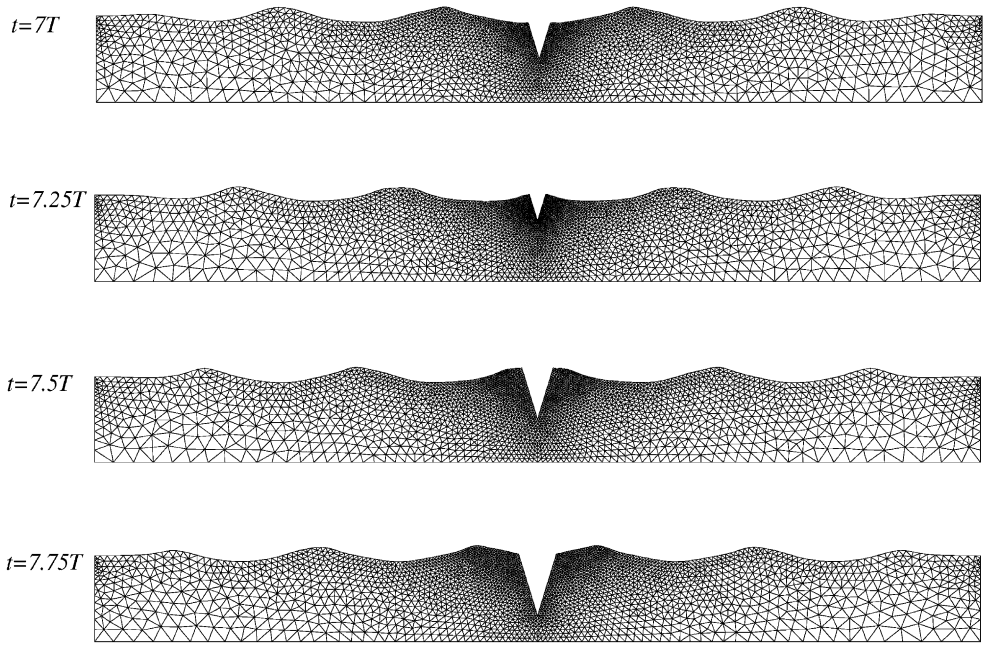

Fig. 28. Meshes in the case of $h = 2d$ and $A/d = 0.4$.

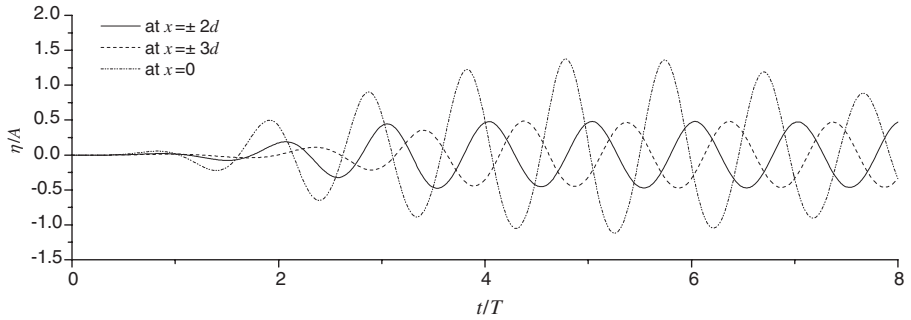

Fig. 29. Wave histories during heave of twin-wedges.

clearly because the location is confined within two bodies. The forces on both wedges should be identical and therefore the results are given only for one wedge. A difference between the twin-wedges and the single wedge in heave is that there is a horizontal force here, as shown in Fig. 31.

5. Conclusions

An unstructured-mesh-based FEM has been developed to analyze fully nonlinear wave interactions with non-wall-sided floating bodies. The mesh allows far more flexibility and more rational distribution of elements in a complex domain and for cases in the complex flow structure. The adoption of the Runge–Kutta method for integration with respect to time provides high-order accuracy without the need for extensive interpolation between results from different meshes. The introduction of the B-Spline to facilitate remeshing has maintained the quality of the mesh throughout the simulation. The use of the energy method for smoothing also removes the restriction of Longuet-Higgins and Cokelet's method to a uniform mesh. Extensive simulation and comparison have demonstrated the effectiveness of the method. More work is, however, needed to deal with cases when the wave overturns and ultimately breaks.

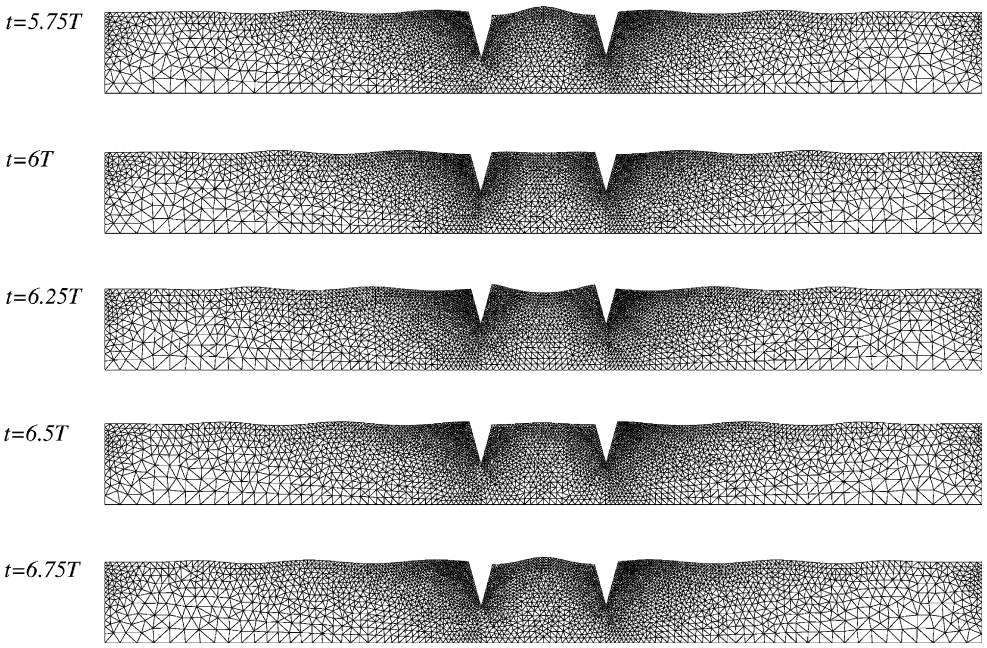

Fig. 30. Meshes for the twin-wedges at different time steps.

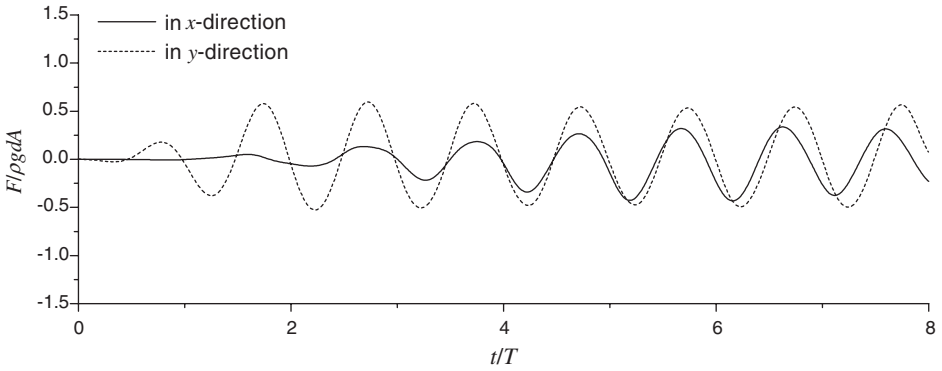

Fig. 31. Force history for wedge one in heave.

Acknowledgements

This work is supported by EPSRC (GR/R26719/01) to which the authors are most grateful.

References

Chung, T.J., 2002. Computational Fluid Dynamics. Cambridge University Press, Cambridge.
Clauss, G.F., Steinhagen, U., 1999. Numerical simulation of nonlinear transient waves and its validation by laboratory data. In: Proceeding of the ninth International Offshore and Polar Engineering Conference, Brest, France, vol. 3, pp. 368–375.
Dale, N., 1998. C++ plus Data Structures. Jones and Bartlett Publishers, Sudbury, MA.
Engeln-Müllges, G., Uhlig, F., 1996. Numerical Algorithms with C. Springer, New York.

Greaves, D.M., Borthwick, A.G.L., Wu, G.X., Eatock Taylor, R., 1997. A moving boundary finite element method for fully nonlinear wave simulations. Journal of Ship Research 41, 181–194.

Hecht, F., 1998. BAMG: Bidimensional anisotropic mesh generator. Website: http://www-rocq1.inria.fr/gamma/cdrom/www/bamg/eng.htm.

Hu, P.X., Wu, G.X., Ma, Q.W., 2002. Numerical simulation of nonlinear wave radiation by a moving vertical cylinder. Ocean Engineering 29, 1733–1750.

Isaacson, M., Ng, J.Y.T., 1993. Time-domain second-order wave radiation in two-dimension. Journal of Ship Research 37, 25–33.

Lin, W.M., Newman, J.N., Yue, D.K., 1984. Nonlinear forced motions of floating bodies. In: Proceedings of the 15th Symposium on Naval Hydrodynamics, Hamburg, Germany, pp. 33–47.

Longuet-Higgins, M.S., Cokelet, E.D., 1976. The deformation of steep surface waves on water, I. A numerical method of computations. Proceedings of the Royal Society of London, A 350, 1–26.

Ma, Q.W., Wu, G.X., Eatock Taylor, R., 2001a. Finite element simulation of fully nonlinear interaction between vertical cylinders and steep waves. Part 1: Methodology and numerical procedure. International Journal for Numerical Methods in Fluids 36, 265–285.

Ma, Q.W., Wu, G.X., Eatock Taylor, R., 2001b. Finite element simulation of fully nonlinear interaction between vertical cylinders and steep waves. Part 2: Numerical results and validation. International Journal for Numerical Methods in Fluids 36, 287–308.

Robertson, I., Sherwin, S., 1999. Free-surface flow simulation using hp/spectral elements. Journal Computational Physics 155, 26–53.

Robertson, I., Sherwin, S.J., Graham, J.M.R., 2004. Comparison of wall boundary conditions for numerical viscous free surface flow simulation. Journal of Fluids and Structures 19, 525–542.

Tanizawa, K., Swada, H., 1996. A numerical method for nonlinear simulation of 2-D body motion in waves by means of BEM. Journal of the Society of Naval Architecture of Japan 166, 311–319.

Turnbull, M.S., Borthwick, A.G.L., Eatock Taylor, R., 2003. Wave-structure intersection using coupled structured-unstructured finite element meshes. Applied Ocean Research 25, 63–77.

Wang, C.Z., Khoo, B.C., 2005. Finite element analysis of two-dimensional nonlinear sloshing problems in random excitations. Ocean Engineering 32, 107–133.

Westhuis, J.H., 2001. The numerical simulation of nonlinear waves in a hydrodynamic model test basin. Ph.D. Thesis, University of Twente, The Netherlands.

Wu, G.X., 1993. A note on hydrodynamic forces on body submerged below a free surface. Applied Ocean Research 15, 371–372.

Wu, G.X., 2000. A note on non-linear hydrodynamic force on a floating body. Applied Ocean Research 22, 315–316.

Wu, G.X., 2006. Numerical simulation of water entry of twin-wedges. Journal of Fluids and Structures 22, 99–108.

Wu, G.X., Eatock Taylor, R., 1994. Finite element analysis of two-dimensional non-linear transient water waves. Applied Ocean Research 16, 363–372.

Wu, G.X., Eatock Taylor, R., 1995. Time stepping solution of the two-dimensional nonlinear wave radiation problem. Ocean Engineering 22, 785–798.

Wu, G.X., Eatock Taylor, R., 1996. Transient motion of floating body in steep water waves. In: Proceedings of the 11th International Workshop on Water Waves and Floating Bodies, Hamburg.

Wu, G.X., Eatock Taylor, R., 2003. The coupled finite element and boundary element analysis of nonlinear interactions between waves and bodies. Ocean Engineering 30, 387–400.

Wu, G.X., Hu, Z.Z., 2004. Simulation of nonlinear interactions between waves and floating bodies through a finite element based numerical tank. Proceedings of the Royal Society of London A 460, 2797–2817.

Wu, G.X., Sun, H., He, Y.S., 2004. Numerical simulation and experimental study of water entry of a wedge in free fall motion. Journal of Fluids and Structures 9, 277–289.

Zhu, X.X., 2000. Modeling of Free-Formed Curves and Surfaces (in Chinese). Science Press, Beijing.

Zhu, G., Borthwick, A.G.L., Eatock Taylor, R., 2001. A finite element model of interaction between viscous free surface waves and submerged cylinders. Ocean Engineering 28, 989–1008.